Electronic Supplementary Material (ESI) for Journal of Materials Chemistry A.

Supporting Information

Asymmetric Gold Nanodimer Arrays: Electrostatic Self-assembly and SERS Activity

Yuanhui Zheng, Lorenzo Rosa, Thibaut Thai, Soon Hock Ng, Daniel E Gómez, Hiroyuki Ohshima and Udo Bach

1. Determination of ionic strength of air-equilibrated Millipore™ water

When Millipore^{TM} water is exposed to air, it keeps absorbing CO_2 and thereby increasing the ionic strength and decreasing pH. Technically, we can calculate the ionic strength of Millipore^{TM} water if we can measure its pH using a pH meter. Since most of pH meters are not designed for measuring pH of a low ionic strength solution, it is extremely difficult to get an accurate pH of Millipore^{TM} water. Here, we used a calibration curve method to determine the ionic strength of the air-equilibrated Millipore™ water that is used for the self-assembly of AuNP dimers. To create a calibration curve, we prepared a set of NaCl solutions with known concentrations and measured their conductivities using a Malvern Zeta Nanosizer. The results are shown in Figure S1.

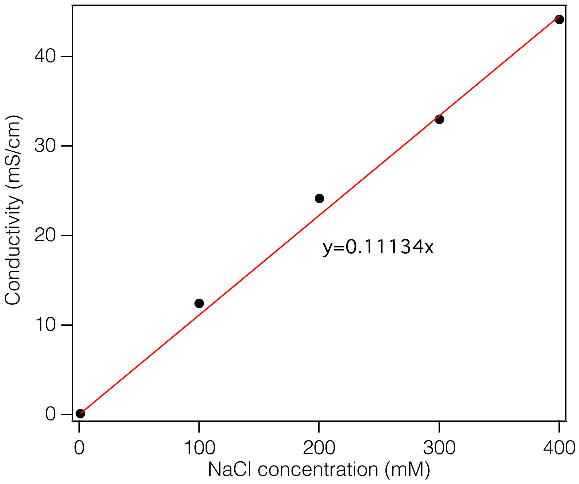

Figure S1. Relationship between the conductivity and ionic strength of sodium chloride solutions made from fresh Millipore™ water.

The relationship between the conductivity and ionic strength is given by

$$\rho \approx 0.11134 \times I \quad (1)$$

The conductivity of the air-equilibrated Millipore™ water is measured to be 0.00148 ± 0.00013 mS/cm. According to eq. (1), the ionic strength of the air-equilibrated Millipore™ water is calculated to be13.3 ± 1.2 µM.

2. Interaction energy calculation based on DLVO theory

To understand the electrostatically driven assembly more clearly, we applied DLVO theory[1] to calculate the interaction energies between a TMAC-AuNP and a surface-confined DNA-AuNP. When a TMAC-AuNP approaches a DNA-AuNP at an angle perpendicular to the APTES modified substrate, the TMAC-AuNP is repelled electrostatically by the background positive charge of the substrate, but is also attracted by both the negative charge of the DNA-AuNP and the van der Waals attraction forces (at shorter distances) from the DNA-AuNP and the substrate. The total interaction energy (E_{total}) between the positively charged NP and the substrate with negatively charged NP is the sum of the contributions of the electrostatic interaction energy (E_e) and the van der Waals energy. It can be expressed as

$$E_{total} = E_e + E_{vdw} = (E_{e,r} + E_{e.a}) + E_{vdw} \qquad (2)$$

The electrostatic repulsion ($E_{e,r}$) and attraction ($E_{e,a}$) energies can be calculated using a linear superposition approximation that can be expressed as:[2-4]

$$E_{e,r} = 4\pi\varepsilon_0\varepsilon_r(k_BT/e)^2 a^+ Y^+_{Au} Y^+_{APTES} \exp(-\kappa z) \qquad (3)$$

and

$$E_{e,a} = 4\pi\varepsilon_0\varepsilon_r(k_BT/e)^2 a^+ a^- /(z + a^+ - a^-) Y^+_{Au} Y^-_{Au} \exp[(-\kappa(z - 2a^-)] \qquad (4)$$

where ε_o is the permittivity of free space, ε_r the relative dielectric constant of water, $a^{+,-}$ the radii of AuNPs ($^+$: TMAC-AuNP; $^-$: DNA-AuNP), k_B the Boltzmann constant, T the absolute temperature, e the unit charge of an electron, z the particle-substrate distance, Y the scaled effective surface potential and κ the Debye-Hückel parameter. The scaled effective surface potentials, Y, can be obtained using the approximation developed by Ohshima to solve the nonlinear Poisson-Boltzmann equations.[5,6]

The Debye-Hückel parameter κ of the electrolyte solution is related to its ionic strength (I) by

$$\kappa = \left(\frac{2000 N_A e^2 I}{\varepsilon_r \varepsilon_o k_B T}\right)^{1/2} \qquad (5)$$

where ε_r is the relative permittivity of water, ε_o the permittivity of vacuum (8.854×10^{-12} F/m), k_B the Boltzmann constant (1.381×10^{-23} J/K), T the absolute temperature, e the elementary unit charge (1.602×10^{-19} C), and N_A the Avogadro number (6.022×10^{23} mol^{-1}).

Now the potential distribution $\psi(r)$ at position r around a spherical particle of radius a can be expressed in terms of its effective surface potential ψ_{eff} as

$$\psi(r) = \psi_{eff} \frac{a}{r} e^{-\kappa(r-a)} \qquad (6)$$

An approximate expression of the effective surface potential ψ_{eff} of a spherical particle in a 1-1 symmetrical electrolyte solution is expressed in terms of the particle surface potential ψ_o as[5, 7]

$$\psi_{\mathrm{eff}} = \frac{kT}{e} \frac{8\tanh\left(\dfrac{e\psi_{\mathrm{o}}}{4kT}\right)}{1+\left\{1-\dfrac{2\kappa a+1}{(\kappa a+1)^2}\tanh^2\left(\dfrac{e\psi_{\mathrm{o}}}{4kT}\right)\right\}^{1/2}} \quad (7)$$

The following scaled (dimensionless) quantities are introduced. The scaled surface potential is given by

$$Y_{\mathrm{o}} = \frac{e}{kT}\psi_{\mathrm{o}} \quad (8)$$

and the scaled effective surface potential by

$$Y_{\mathrm{eff}} = \frac{e}{kT}\psi_{\mathrm{eff}} = \frac{8\tanh\left(\dfrac{Y_{\mathrm{o}}}{4}\right)}{1+\left\{1-\dfrac{2\kappa a+1}{(\kappa a+1)^2}\tanh^2\left(\dfrac{Y_{\mathrm{o}}}{4}\right)\right\}^{1/2}} \quad (9)$$

For a planar surface ($\kappa a \to \infty$) carrying surface potential ψ_{o} (and thus the scaled surface potential $Y_{\mathrm{o}} = e\psi_{\mathrm{o}}/kT$) in a 1-1 aqueous electrolyte solution, it follows from the eqs. (7) and (9) that the effective surface potential ψ_{eff} and the scaled effective surface potential Y_{eff} are given by

$$\psi_{\mathrm{eff}} = \frac{4kT}{e}\tanh\left(\frac{e\psi_{\mathrm{o}}}{4kT}\right) \quad (10)$$

$$Y_{\mathrm{eff}} = \frac{e}{kT}\psi_{\mathrm{eff}} = 4\tanh\left(\frac{Y_{\mathrm{o}}}{4}\right) \quad (11)$$

Determination of Surface Potentials of AuNPs and APTES Modified Substrate: For a spherical NP (radius: *a*), the electrophoretic mobility is defined by[8]

$$\mu \equiv \frac{v}{E} = \frac{\varepsilon\zeta}{6\pi\eta} \quad (12)$$

where v is the steady velocity, E the electric field magnitude, and η the shear viscosity of water. This is known as the Hückel-Onsager equation and expected to be valid for low ionic strength ($\kappa \to 0$) and small particles ($a \to 0$). The diameters of the AuNP conjugates used in this work are in the range of 30 nm-60 nm. Hence the zeta potentials of DNA-AuNPs and TMAC-AuNPs listed in Table 1 are considered as their surface potentials for the scaled effective surface potential calculation (see Table 2-6 for the calculated results). The zeta potential measurements for all samples were carried out in the air-equilibrated Millipore™ water.

Table 1. Surface potential of AuNP conjugates.

	30 nm DNA-AuNPs	TMAC-AuNPs			
		30 nm	40 nm	50 nm	60 nm
$\Psi_o \approx \zeta$ /mV	-69 ± 6	+67 ± 2	+60 ± 6	+59 ± 6	+54 ± 4

Table 2. Effective surface potential of 30 nm DNA-AuNP conjugates.

T / K	ε_r	I / μM	a / nm	κa	ψ_o	Y_o	ψ_{eff}	Y_{eff}
					/mV			
298.15	78.55	13.3	15	0.180	-69	-2.69	-66.3	-2.58
298.15	78.55	15.0	15	0.191	-69	-2.69	-66.3	-2.58
298.15	78.55	20.0	15	0.220	-69	-2.69	-66.3	-2.58
298.15	78.55	25.0	15	0.246	-69	-2.69	-66.2	-2.58
298.15	78.55	25.8	15	0.250	-69	-2.69	-66.2	-2.58
298.15	78.55	28.3	15	0.262	-69	-2.69	-66.2	-2.58
298.15	78.55	30.0	15	0.270	-69	-2.69	-66.2	-2.58
298.15	78.55	33.3	15	0.284	-69	-2.69	-66.1	-2.57
298.15	78.55	35.0	15	0.292	-69	-2.69	-66.1	-2.57
298.15	78.55	38.3	15	0.305	-69	-2.69	-66.1	-2.57
298.15	78.55	40.0	15	0.312	-69	-2.69	-66.1	-2.57

Table 3. Effective surface potential of 30 nm TMAC-AuNP conjugates

T / K	ε_r	I / μM	a / nm	κa	ψ_o	Y_o	ψ_{eff}	Y_{eff}
					/mV			
298.15	78.55	13.3	15	0.180	67	2.61	64.6	2.51
298.15	78.55	15.0	15	0.191	67	2.61	64.5	2.51
298.15	78.55	20.0	15	0.220	67	2.61	64.5	2.51
298.15	78.55	25.0	15	0.246	67	2.61	64.4	2.51
298.15	78.55	25.8	15	0.250	67	2.61	64.4	2.51
298.15	78.55	30.0	15	0.270	67	2.61	64.4	2.51
298.15	78.55	35.0	15	0.292	67	2.61	64.4	2.51
298.15	78.55	40.0	15	0.312	67	2.61	64.3	2.50

Table 4. Effective surface potential of 40 nm TMAC-AuNP conjugates.

T / K	ε_r	I / μM	a / nm	κa	ψ_o	Y_o	ψ_{eff}	Y_{eff}
					/mV			
298.15	78.55	13.3	20	0.240	60	2.34	58.1	2.26
298.15	78.55	15.0	20	0.255	60	2.34	58.1	2.26
298.15	78.55	20.0	20	0.294	60	2.34	58.1	2.26
298.15	78.55	25.0	20	0.329	60	2.34	58.0	2.26
298.15	78.55	28.3	20	0.350	60	2.34	58.0	2.26
298.15	78.55	30.0	20	0.360	60	2.34	58.0	2.26
298.15	78.55	35.0	20	0.389	60	2.34	58.0	2.26
298.15	78.55	40.0	20	0.416	60	2.34	57.9	2.25

Table 5. Effective surface potential of 50 nm TMAC-AuNP conjugates.

T / K	ε_r	I / μM	a / nm	κa	ψ_o	Y_o	ψ_{eff}	Y_{eff}
					/mV			
298.15	78.55	13.3	25	0.300	59	2.30	57.2	2.23
298.15	78.55	15.0	25	0.318	59	2.30	57.2	2.22
298.15	78.55	20.0	25	0.367	59	2.30	57.1	2.22
298.15	78.55	25.0	25	0.411	59	2.30	57.0	2.22
298.15	78.55	30.0	25	0.450	59	2.30	57.0	2.22
298.15	78.55	33.3	25	0.474	59	2.30	56.9	2.22
298.15	78.55	35.0	25	0.486	59	2.30	56.9	2.22
298.15	78.55	40.0	25	0.520	59	2.30	56.9	2.21

Table 6. Effective surface potential of 60 nm TMAC-AuNP conjugates

T / K	ε_r	I / μM	a / nm	κa	ψ_o	Y_o	ψ_{eff}	Y_{eff}
					/mV			
298.15	78.55	13.3	30	0.360	54	2.10	52.5	2.04
298.15	78.55	15.0	30	0.382	54	2.10	52.5	2.04
298.15	78.55	20.0	30	0.441	54	2.10	52.4	2.04
298.15	78.55	25.0	30	0.493	54	2.10	52.4	2.04
298.15	78.55	30.0	30	0.540	54	2.10	52.3	2.04
298.15	78.55	35.0	30	0.583	54	2.10	52.3	2.04
298.15	78.55	38.3	30	0.610	54	2.10	52.3	2.03
298.15	78.55	40.0	30	0.624	54	2.10	52.3	2.03

For a planar surface ($\kappa a \to \infty$), the electrophoretic mobility is defined by[8]

$$\mu \equiv \frac{v}{E} = \frac{\varepsilon\zeta}{4\pi\eta} \quad (13)$$

This is known as the Helmholtz-Smoluchowski equation. When the depth (d) of the cell used for the zeta potential measurement (i.e. the separation between two planar surfaces) is much longer than the Debye length (κ^{-1}), the plane of shear is expected to be close to the outer Helmholtz plane (i.e. Stern plane). Therefore one expects the zeta potential of a planar surface to be approximately equal to the surface potential. The zeta potential measurement of the APTES modified substrate was carried out in an electrolyte solution with 10 mM NaCl ($\kappa^{-1} = 0.304$ nm) using a clamping cell ($d \approx 0.1$ mm; $W = 50$ mm, $L = 20$ mm) and found to be 19.8 ± 4.0 mV. This value is considered as the surface potential of APTES modified substrate for the scaled effective surface potential calculation (see Table 7 for the calculated results).

Table 7. Effective surface potential of APTES modified substrate

T / K	ε_r	I / μM	κa	ψ_o	Y_o	ψ_{eff}	Y_{eff}
				/mV			
298.15	78.55	13.3	∞	19.8	0.771	19.6	0.761
298.15	78.55	15.0	∞	19.8	0.771	19.6	0.761
298.15	78.55	20.0	∞	19.8	0.771	19.6	0.761
298.15	78.55	25.0	∞	19.8	0.771	19.6	0.761
298.15	78.55	25.8	∞	19.8	0.771	19.6	0.761
298.15	78.55	30.0	∞	19.8	0.771	19.6	0.761
298.15	78.55	33.3	∞	19.8	0.771	19.6	0.761
298.15	78.55	35.0	∞	19.8	0.771	19.6	0.761
298.15	78.55	38.3	∞	19.8	0.771	19.6	0.761
298.15	78.55	40.0	∞	19.8	0.771	19.6	0.761

The van der Waals attraction energy (E_{vdw}) can expressed as follows[9,10]

$$E_{vdw} = -\frac{A_{Au}}{6}\Big[\frac{2a^+a^-}{2(a^+ + a^-)(z-2a^-)+(z-2a^-)^2} + \frac{2a^+a^-}{4a^+a^- + 2(a^+ + a^-)(z-2a^-)+(z-2a^-)^2}$$

$$+ \ln\frac{2(a^+ + a^-)(z-2a^-)+(z-2a^-)^2}{4a^+a^- + 2(a^+ + a^-)(z-2a^-)+(z-2a^-)^2}\Big] - \frac{A_{sub}}{6}\Big[\frac{a^+}{z} + \frac{a^+}{2a^+ + z} + \ln\frac{z}{2a^+ + z}\Big] \quad (14)$$

where A_{Au} *and* A_{sub} are the Hamaker constants for the system Au/TMAC/water/DNA/Au and Au/TMAC/water/APTES/SiO_2, the reported values of which are 2.5×10^{-19} J and 5.7×10^{-20} J, respectively.[11,12] The first term corresponds to the van der Waals interaction energy between the TMAC-AuNP and DNA-AuNP. The second term represents the van der Waals interaction between the TMAC-AuNP and the substrate.

3. SEM micrograph and nearest-neighbor distance of DNA-AuNP arrays

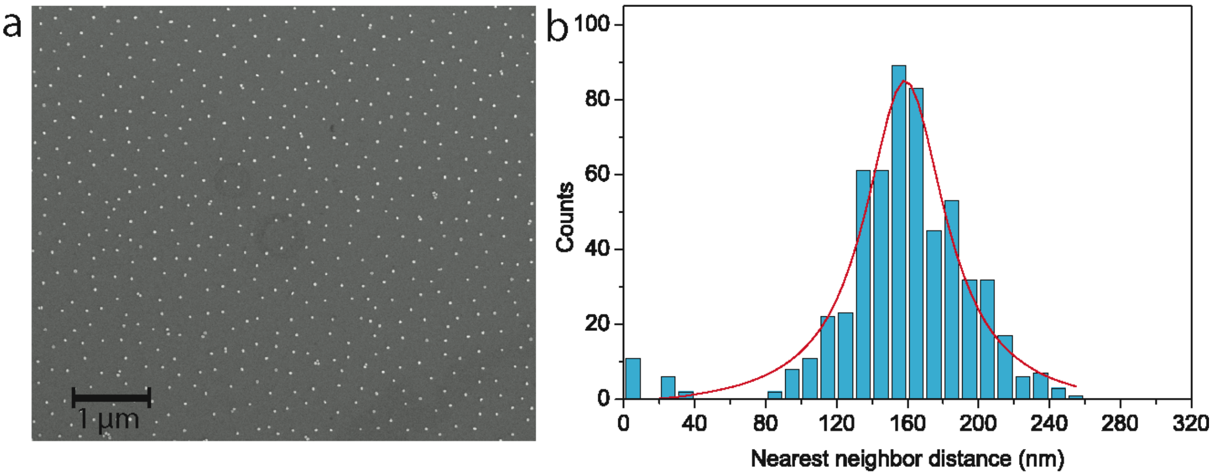

Figure S2. (a) Typical low-magnification SEM micrograph of 30 nm DNA-AuNP arrays on a silica-coated silicon substrate fabricated through electrostatic self-assembly. (b) Distance analysis of the particles shown in panel a: the distance between each DNA-AuNP and its nearest neighbor was measured (edge-to-edge) using image analysis. The positions of the self-assembled nanoparticles shown in panel a) were determined using ImageJ (Rasband, W.S., ImageJ, U. S. National Institutes of Health, Maryland, USA, http://imagej.nih.gov/ij/, 1997-2011). To achieve this the 'Threshold' tool was used with a lower and upper intensity threshold of 144 and 255 respectively for the identification of particles. The 'Analyze Particles' tool was used to determine the coordinates of the center of gravity for each particle. The coordinates were then transferred to R (R: A language and environment for statistical computing. R Foundation for Statistical Computing, Vienna, Austria. ISBN 3-900051-07-0, http://www.Rproject.org.) and the nearest neighbor distances determined using the "nndist" routine of the "spatstat" library (A. Baddeley and R. Turner (2005). Spatstat: an R package for analyzing spatial point patterns. Journal of Statistical Software 12 (6), 1-42. ISSN: 1548-7660. URL: www.jstatsoft.org).

4. Self-assembly of 30 nm TMAC-AuNPs onto DNA-AuNPs under salt free conditions

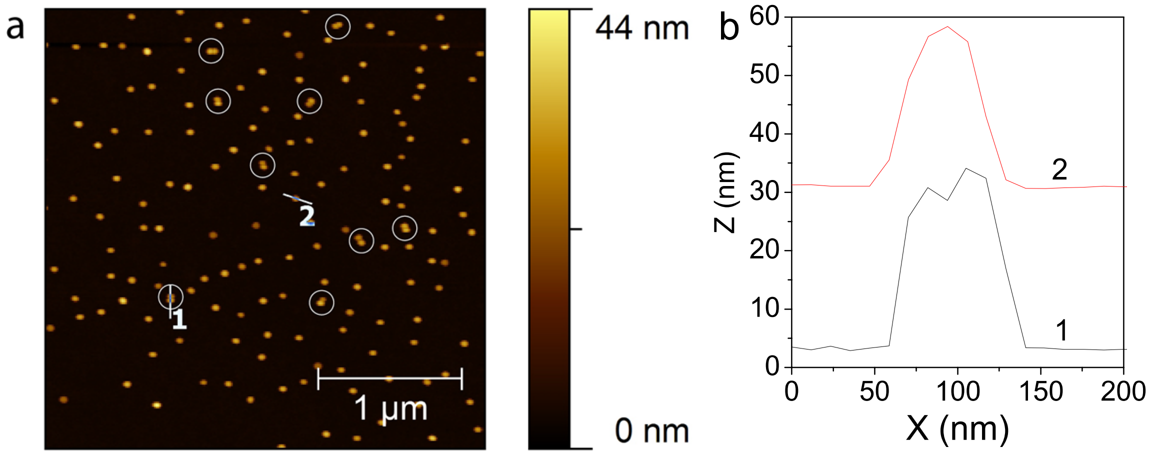

Figure S3. (a) Typical AFM micrograph of 30-30 nm dimers assembled in air-equilibrated Millipore™ water (ionic strength ≈ 13.3 µM) and (b) cross-section profiles of the assemblies 1 and 2 shown in panel a. All dimers in the AFM micrograph are highlighted with circles and their yield is found to be ~ 6%.

5. The effect of salt concentration on the self-assembly of AuNP dimers

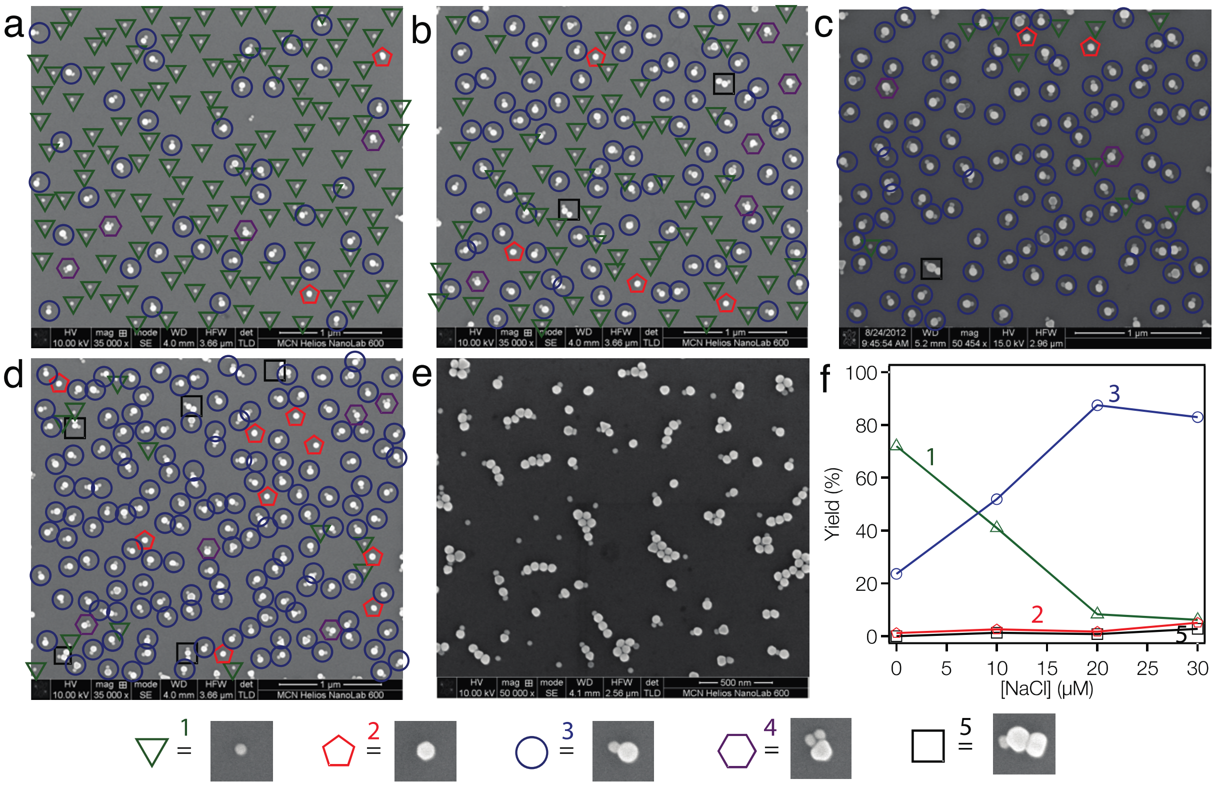

Figure S4. Typical SEM images of 30-60 nm dimers synthesized at different NaCl concentrations: (a) 0 µM (i.e. in air-equilibrated Millipore™ water, ionic strength ≈ 13.3 µM), (b) 10 µM (ionic strength ≈ 23.3 µM), (c) 20 µM (ionic strength ≈ 33.3 µM), (d) 30 (ionic strength ≈ 43.3 µM) and (e) 1 mM (ionic strength ≈ 1.0133 mM); and (f) SEM image-based statistic analysis of the resulting AuNP assemblies as a function of NaCl concentration.

6. Calculated energy barrier for the formation of trimers

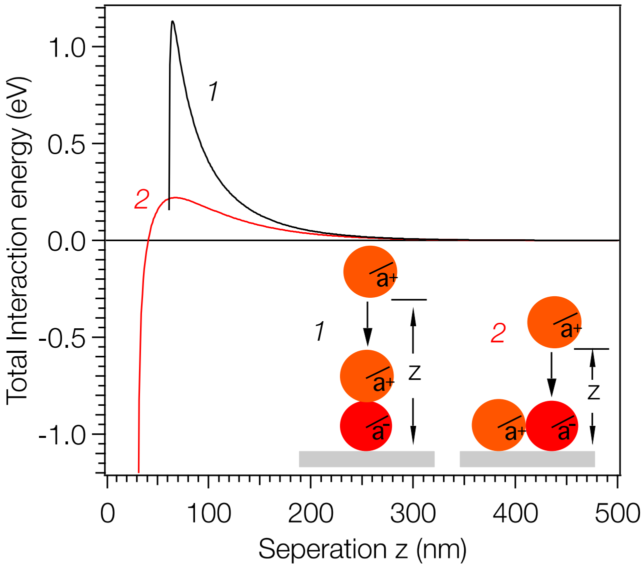

Figure S5. Calculated energy barriers for the formation of trimers based on the 30 nm AuNP system. We calculated the total interaction energy for a TMAC-AuNP approaching to a 30-30 nm dimer on the substrate (see the inset). Two different dimer configurations were adopted for the interaction energy calculations: (1) vertical dimers and (2) horizontal dimers. The calculations were conducted assuming that the TMAC-AuNP is approaching to the negatively charged AuNP at an angle perpendicular to the substrate. The calculated data show that the successful adsorption of the second TMAC-AuNP onto horizontal dimers and vertical dimers requires to overcome an energy barrier of 1.1 eV and 0.2 eV, respectively. These high-energy barrier indicate that trimer formation yields should be low.

7. UV-vis absorption spectra of 30-60 nm dimers before and after drying

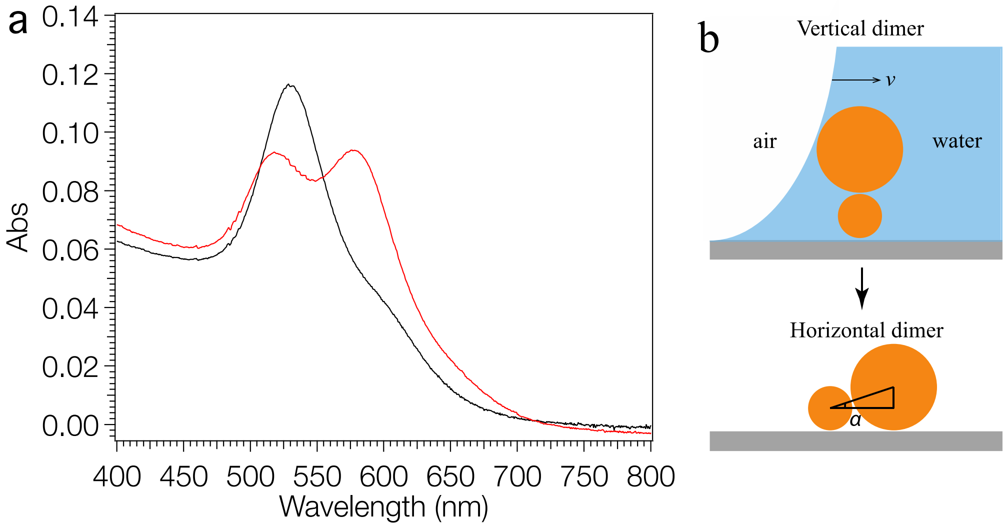

Figure S6. (a) UV-vis spectra of 30-60 nm AuNP dimers before (black curve) and after (red curve) drying. The dimers were assembled in the presence of 25 μM NaCl at 25 °C for 3 h. (b) A schematic representation of the formation of horizontal dimers. α is the angle used to describe the slight vertical orientation of the asymmetric dimers. Prior to drying, a major absorption peak at 525 nm with a shoulder located at 610 nm is observed. The major peak is attributed to the excitation of the transverse plasmon mode of the dimers, while the shoulder might be due to the excitation of the longitudinal plasmon mode of the dimers. After drying, the intensity of the peak at longer wavelength increases significantly. With unpolarized light illumination, only the transverse plasmon mode can be efficiently excited for the vertical dimers. For the horizontal dimers, both the transverse and axial modes can be excited (see Section 9 of Supporting Information for details).

8. SEM image-based statistic analysis of AuNP dimers

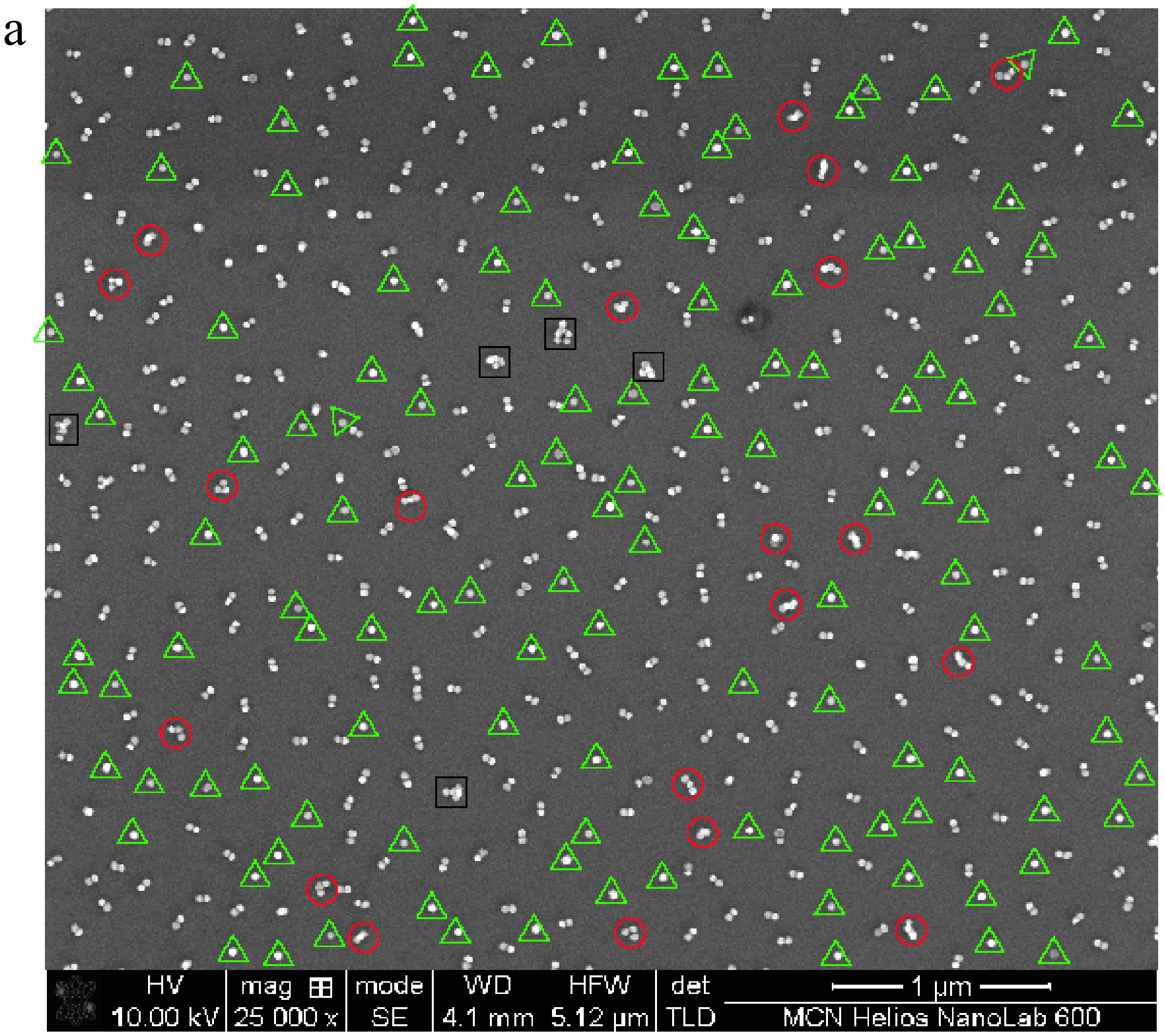

Types of assemblies	Counts	Percentage (%)
Monomers	128	27.6
Dimers	311	67.0
Trimers	20	4.3
Large aggregates	5	1.1

b

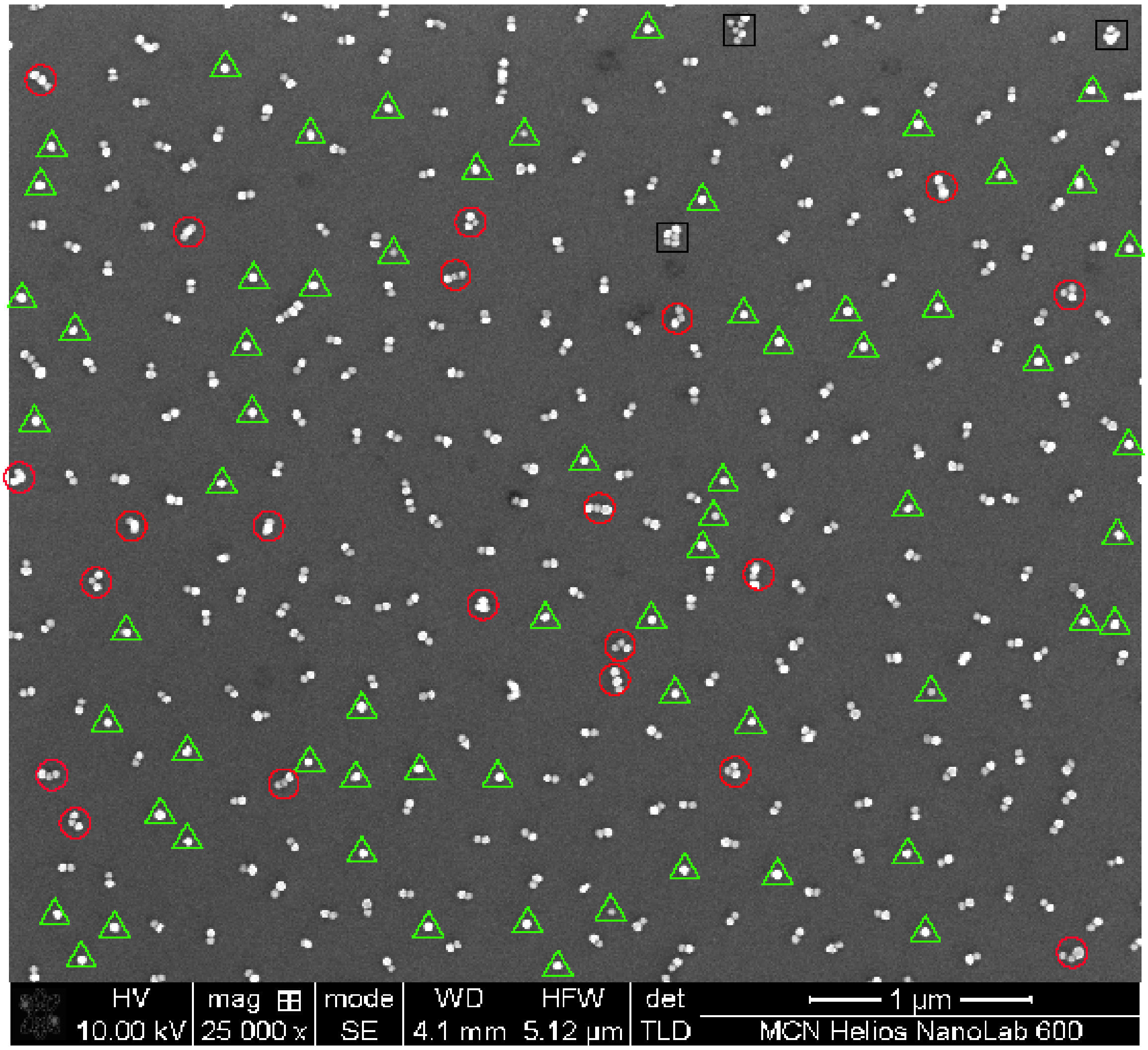

Types of assemblies	Counts	Percentage (%)
Monomers	65	20.2
Dimers	233	72.6
Trimers	20	6.2
Large aggregates	3	1.0

c

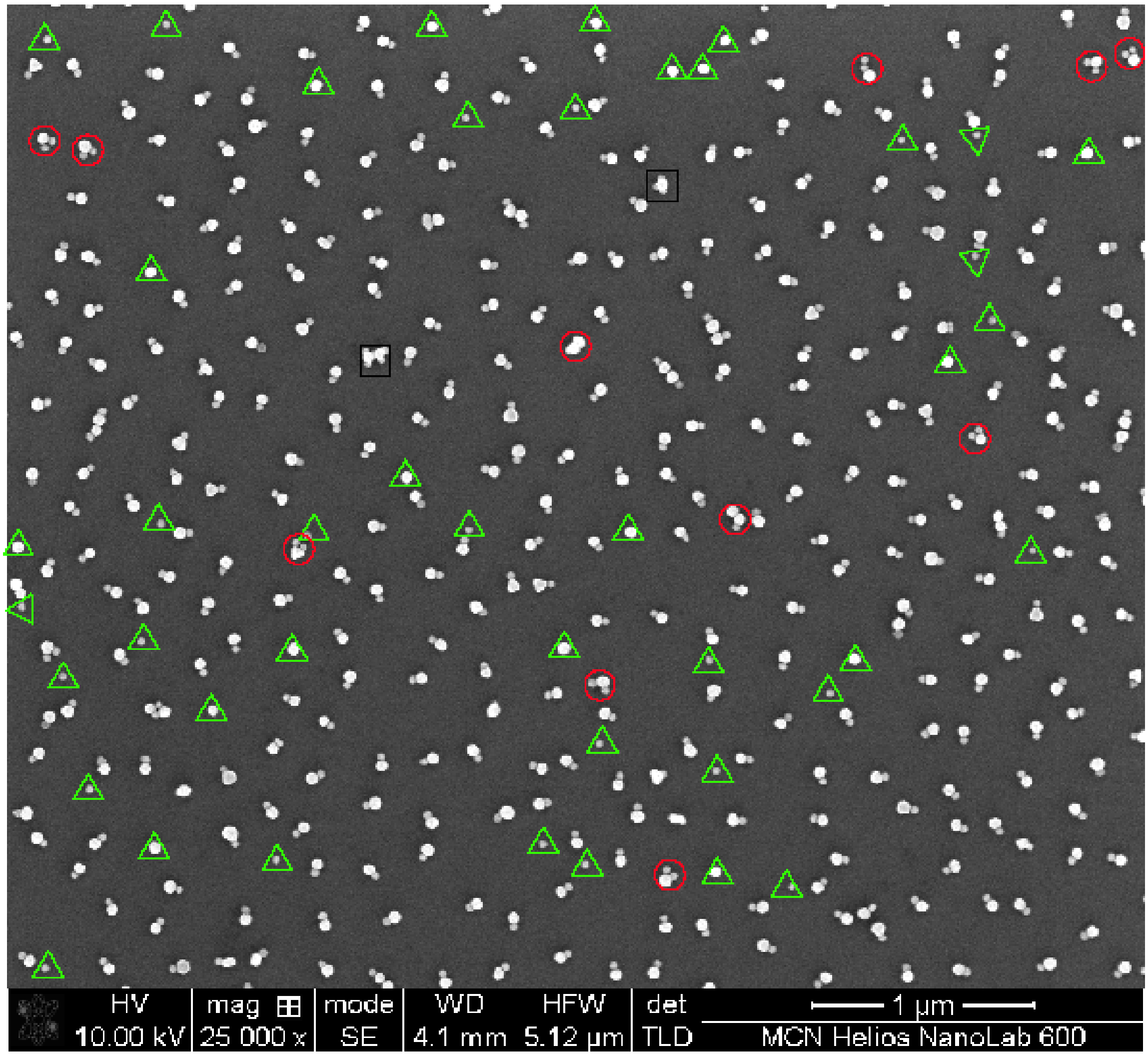

Types of assemblies	Counts	Percentage (%)
Monomers	43	11.3
Dimers	324	85.3
Trimers	12	2.9
Large aggregates	2	0.5

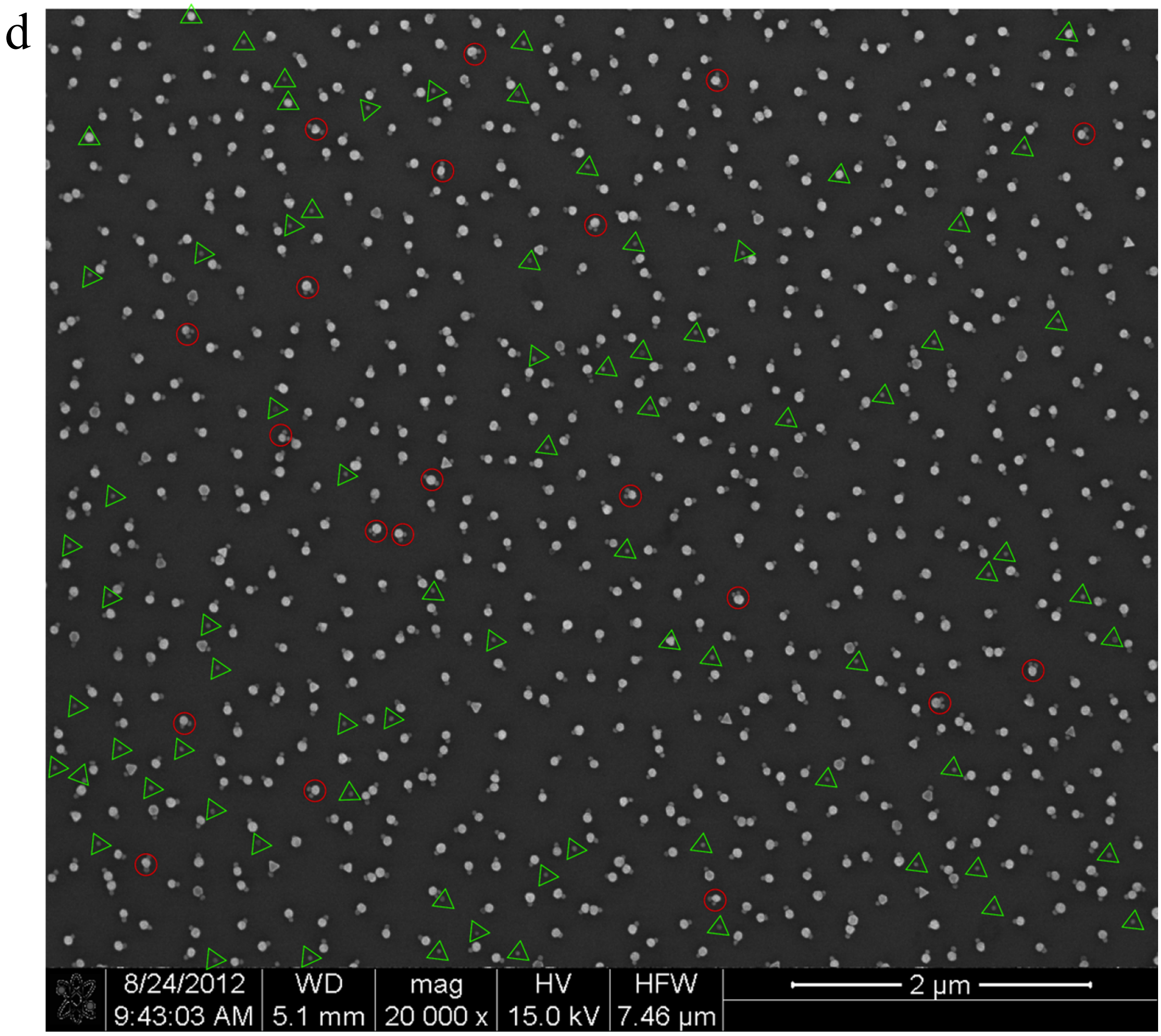

Types of assemblies	Counts	Percentage (%)
Monomers	77	9.4
Dimers	718	88.1
Trimers	20	2.5
Large aggregates	0	0

Figure S7. Typical low magnification SEM micrographs of arrays of AuNP dimers: (a) 30-30 nm (symmetric) dimers, (b) 30-40 nm, (c) 30-50 nm and (d) 30-60 nm dimers (panel b-d: asymmetric dimers). The resulting assemblies are composed of monomers (highlighted with triangles), dimers, trimers (highlighted with circles) and large aggregates containing more than 3 particles (highlighted with squares). As discussed in the manuscript, there are two configurations for the AuNP dimers: vertical dimers and lateral dimers. For the statistical analyses of the configuration distribution of the assemblies shown here, we consider all vertical dimers as monomers. The statistical results are summarized in the fourth column of Figure 2 in the main text.

9. Modeling of optical properties of AuNP dimers

9.1 Electrostatic Eigenmode Method

To describe semi-quantitatively the surface plasmon resonances of the sphere dimers, we apply the Electrostatic Eigenmode Method (EEM),[13,14] a theory wherein a metal particle, *p*, has a set of self-sustained surface charge oscillations, $\sigma_{p,m}$, that satisfy an eigenvalue equation:

$$\sigma_{p,m}(\vec{r}) = \frac{\gamma_{p,m}}{2\pi} \oint \sigma_{p,m}(\vec{r}) \frac{\partial G(\vec{r},\vec{r}\,')}{\partial n} dS \qquad (15)$$

where the surface integral is carried out for the closed surface *S* describing the particle(s), *n* is the normal to this surface, $G(\vec{r},\vec{r}\,')$ is the electrostatic Green function:

$$G(\vec{r},\vec{r}\,') = \frac{1}{|\vec{r}-\vec{r}\,'|} \qquad (16)$$

and $\Upsilon_{p.m}$ is the eigenvalue that dictates the resonance wavelength (frequency, ω) of the surface plasmon modes in the coupled NPs through the following relationship:

$$\varepsilon(\omega_{p,m}) = \varepsilon_b \left(\frac{1+\gamma_{p,m}}{1-\gamma_{p,m}}\right) \qquad (17)$$

Here, $\varepsilon(\omega)$ the metal permittivity and ε_b the permittivity of the surrounding medium, which is assumed to be uniform (i.e. we neglect to first order, the effects of the substrate).[15]

Numerically, the surface of the NP is discretized with an appropriate mesh, a procedure that results in transforming eq. (15) into a matrix equation that is easily solved by using standard numerical methods. The numerical implementation that we have used here is the one developed by Hohenester et al.[16] to solve the boundary element method (BEM) problem. The electrostatic BEM is equivalent to the EEM. In the electrostatic BEM, one solves for surface charge distributions according to the following equation:[16]

$$\Lambda_{p,m}\sigma_{p,m}(\vec{r}) + \oint \sigma_{p,m}(\vec{r}) \frac{\partial G(\vec{r},\vec{r}\,')}{\partial n} dS = 0 \qquad (18)$$

which is formally, equivalent to eq. (15) by noting that

$$\gamma_{p,m} = -\frac{2\pi}{\Lambda_{p,m}} \qquad (19)$$

For the problem of the sphere dimers embedded in a uniform medium, there are in general two types of collective surface plasmon resonances: one plasmon mode that has a net dipole moment along the axis connecting the centers of the spheres (axial or longitudinal mode) and two degenerate modes with dipole moments perpendicular to this axial mode (transverse modes). Due to the close proximity of the NPs, the axial mode requires a logarithmic mesh (in

Figure S8) in order to better describe the tight spatial confinement of the surface charge distributions in the particles. For the transverse modes a uniform mesh was employed, since these modes require a more uniform sampling of the surfaces of the NPs in the direction perpendicular to the axis connecting the spheres.

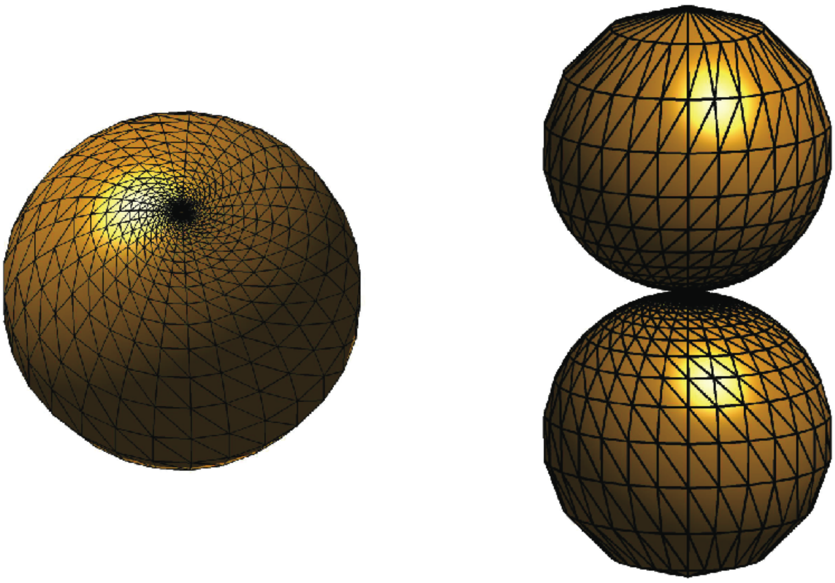

Figure S8. Logarithmic grid employed to solve eq. (15). The grid is densest at one of the poles of the sphere and the aim of using this non-uniform mesh is to better describe the highly localized surface charge distributions expected to occur in closely spaced dimers.

These two types of plasmon modes, the axial and transverse, have two different resonance wavelengths where the axial mode occurs at longer wavelengths than the transverse. For a given dimer, the positions of these resonances depends on: (i) the refractive index of the medium surrounding the particles and (ii) their mutual separation distance. We have fixed the refractive index of the medium to 1.3 ($\varepsilon_b = 1.69$) based on the previous study on the effect of the substrate[17] and its theoretical modeling using the EEM,[15] where it was found that this value closely represents the dielectric environment of metal particles located at an air/glass interface. The determination of the interparticle separation distance was made by a pseudo fitting procedure, where we calculated the plasmon resonance wavelength for a given dimer as a function of interparticle separation distance (Figure S9a) and chose a value that shows the closest agreement to the experimental results. The optical absorption spectrum for an AuNP dimer consists of two bands that originate from the axial and transverse resonances, as exemplified in Figure S9b. The relative contributions of these two bands to the measured spectrum are dependent on the experimental illumination conditions, and in particular, on the orientation of the dimer in relation to the polarization of the incident light beam.

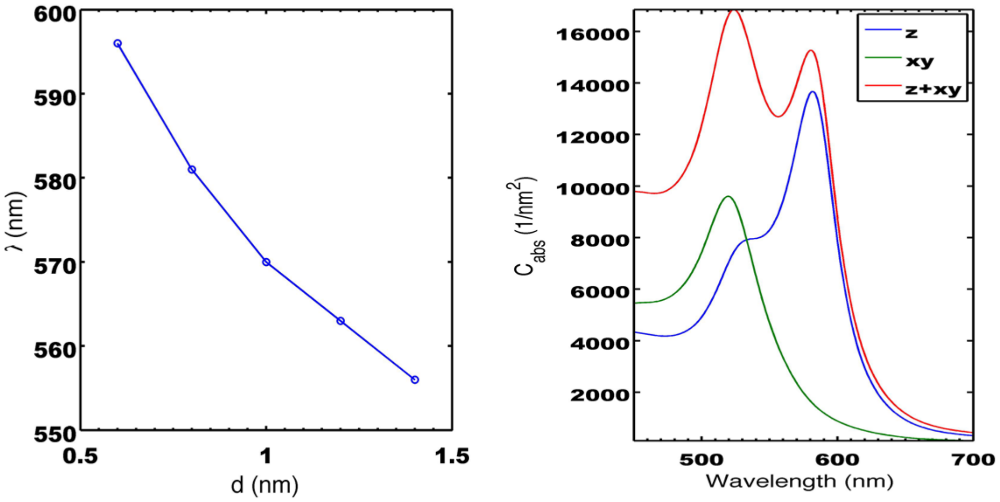

Figure S9. (a) Evolution of the wavelength position of the axial surface plasmon resonance (λ) with interparticle separation distance, *d*. These points were calculated for a 30-60 nm dimer. (b) Calculated absorption cross section (C_{abs}) for a 30-60 nm dimer with a separation distance of 0.8 nm. *z* is the axial mode, *xy* the transverse modes. *z* +*xy* is a simple addition of both spectra.

Table 8. Distribution of the orientation of AuNP dimers on the substrates.[a]

Dimers	Vertical (%)	Horizontal (%)
30-30 nm	24.6	75.4
30-40 nm	16.7	83.3
30-50 nm	3.9	96.1
30-60 nm	1.0	99.0

[a] Data were derived from detailed analysis of AFM images, as exemplified in Figure 2 of the manuscript. “Horizontal” and “Vertical” refer to the two possible orientations of a dimer in relation to the surface normal of the substrate (see Figure S6).

In our experiments, we employed unpolarized monochromatic light and our samples were oriented on the substrates as summarized in Table 8. With incident unpolarized light, only the transverse plasmon mode can be efficiently excited for the vertical dimers, while for the horizontal dimers, both the transverse and axial modes can be excited, as schematically illustrated in Figure S10. Therefore, the absorption spectrum, A_H, of the horizontal dimers is a combination of both excitations given by:

$$A_H = \left[1 + tan(\alpha)\right] A_{xy} + A_z / cos(\alpha) \quad (20)$$

where A_{xy} is the absorption due to the transverse modes, A_z originates from the axial mode, and α is the angle used to describe the slight vertical orientation of the asymmetric dimers (Figure S6b). α is given by:

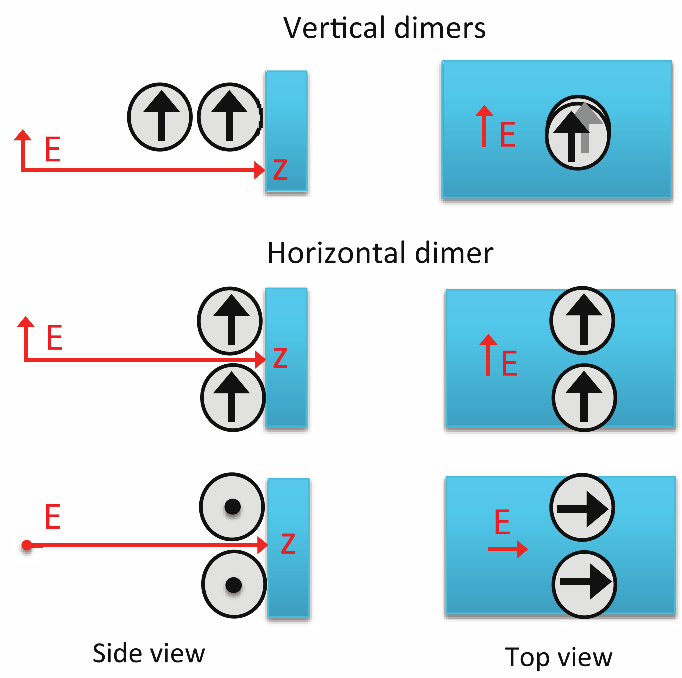

Figure S10. A schematic representation of the surface plasmon excitation for vertical dimers (top panel) and horizontal dimers (bottom panel). With incident unpolarized light (coming from z direction, left panel), only the transverse plasmon mode can be efficiently excited for the vertical dimers, while for the horizontal dimers, both the transverse and axial modes can be excited.

$$sin(\alpha) = \frac{r_2 - r_1}{r_2 + r_1} \quad (21)$$

where r corresponds to the radii of the spheres. However, for a sample containing both vertical and horizontal dimers, the orientation-averaged absorption spectrum $\langle A \rangle$ was calculated using the data of Table 8 according to:

$$\langle A \rangle = VA_{xy} + HA_H \quad (22)$$

where V and H are the "concentrations" of vertical and horizontal dimers, respectively. By following the procedure described, we have produced the normalized absorption spectra shown in Figure 3 of the manuscript, which shows good agreement with the experimental data also shown.

9.2 Three-Dimensional Finite-Difference Time-Domain Method

The absorption cross-section and electromagnetic field enhancement were simulated with the three-dimensional (3D) finite-difference time-domain (3D-FDTD) method, by the Lumerical software.[18] The field enhancement is recorded via a set of electric field monitors crossing the nano-gap on the along the *xy* and *xz* planes, and the simulation is repeated for TMAC-AuNP diameters varying from 30 to 60 nm.

The simulation boundary is lined with perfectly matched layers (PMLs) to avoid spurious reflections, which corresponds to a single dimer on an infinitely wide silica-coated silicon substrate, excited by an x-polarized plane wave source from the top side with wavelength from 400 to 820 nm. To achieve a good hot-spot definition, the domain is discretised with a mesh size of 0.2 nm.

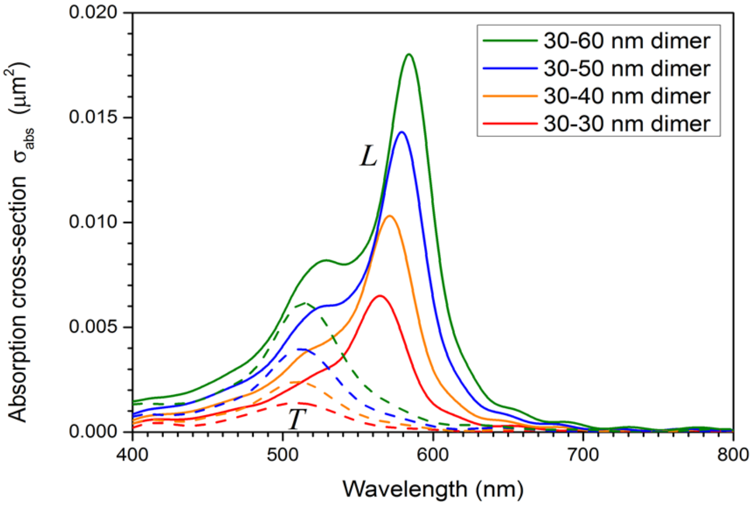

Figure S11. Simulated absorption cross-sections of the dimers with a transverse excitation (dash lines) and a longitudinal excitation (solid lines).

The absorption cross-sections of the dimers have been calculated with a total-field-scattered-field approach[18] by separating scattering from extinction, and they are shown in Figure S11 for the excitation of the horizontal dimer in the transverse direction (T) and in the longitudinal direction (L). The calculation results previously obtained (Figure 3a in the main manuscript) are confirmed and the assumption of the equivalent medium surrounding the particles in the Electrostatic Eigenmode Method is valid. It can be seen that the two resonant modes are well separated for the symmetric dimer, while for the asymmetric ones, the slight vertical orientation of the dimer induces a mode coupling, permitting to excite the T-mode with L-polarization. The T-mode absorption is weaker, having one-third the cross-section of the L-mode.

Table 9. Electric field enhancement at gap center, hot-spot radii, and volume integral of SERS enhancement over the hot spot, for excitation at 782 nm and SERS at 854 nm (1075 cm^{-1})

Type of dimers	λ_L, λ_R (nm)	$\lvert E_{L,max}/E_0\rvert^2$ (norm.)	$\lvert E_{R,max}/E_0\rvert^2$ (norm.)	D (nm)	d (nm)	$\int\lvert E_L/E_0\rvert^2\lvert\ E_R/E_0\rvert^2vdv$ (nm^3)
30-30 nm	782, 854	1100	750	2.1	0.8	2.1×10^6
30-40 nm	782, 854	1500	1050	3.2	0.8	4.7×10^6
30-50 nm	782, 854	2100	1350	3.9	0.85	1.13×10^7
30-60 nm	782, 854	2400	1450	4.5	0.85	1.46×10^7

L: laser, R: Raman.

To understand how the field enhancement and geometry impact on the SERS process, we evaluated the size of the hot spot in mid-gap at the 782 nm laser wavelength, and integrated the light intensity at the laser and Raman wavelengths on the hot-spot volume. The boundary was chosen with a threshold criterion (the integration domain is the region where the local intensity enhancement at the laser wavelength is greater than 10^3; the threshold was determined by fitting to the experimental results in Figure 4(b) in the main manuscript) and the results are shown in Table 9, noting that the hot-spot size, as fitted by an equivalent oblate spheroid of major diameter “D” and minor diameter “d”, constantly increases with core diameter. Thus by this criterion, the integrals of the intensity of excitation and scattering by the analyte increase from 30-30 to 30-60 dimers, and are expected to further increase with core size up to a saturation point to be determined.

10. SEM image of 30-50 nm dimers after Sulfo-SMCC treatment, thiol exchange, UV-ozone treatment and analyte loading

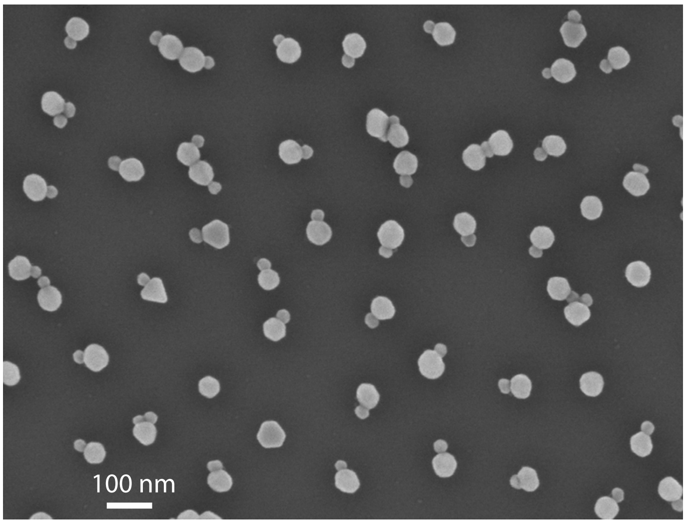

Figure S12. SEM image of 30-50 nm dimers after Sulfo-SMCC treatment, DDT treatment, UV-ozone treatment and analyte loading.

11. UV-vis absorption spectra of 30-60 nm dimers after Sulfo-SMCC treatment, thiol exchange, UV-ozone treatment and analyte loading

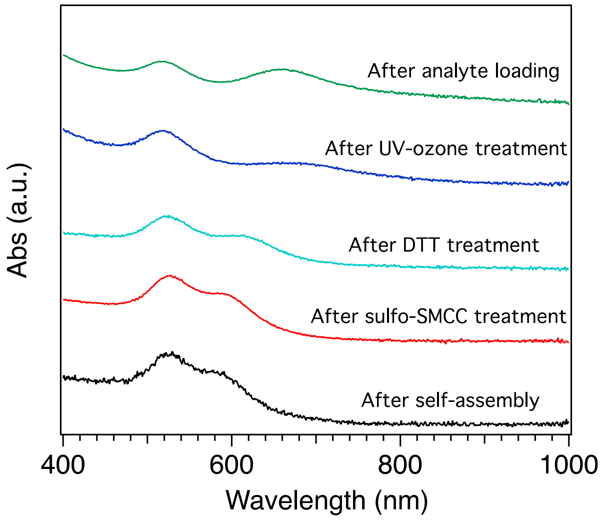

Figure S13. UV-vis absorption spectra of 30-60 nm dimers after Sulfo-SMCC treatment, DDT treatment, UV-ozone treatment and analyte loading.

References

[1] L. C. Ma, R. Subramanian, H. W. Huang, V. Ray, C. U., Kim, S. J. Koh, *Nano Lett.* **2007**, *7*, 439.
[2] G. M. Bell, S. Levine, L. N. McCartney, *J. Colloid Interface Sci.***1970**, *33*, 335.
[3] P. Warszynski, Z. Adamczyk, *J. Colloid Interface Sci.* **1997**, *187*, 283.
[4] Z. Adamczyk, P. Warszynski, *Adv. Colloid Interface Sci.* **1996**, *63*, 41.
[5] H. Ohshima, *J. Colloid Interface Sci.* **1995**, *174*, 45.
[6] H. Ohshima, *J. Colloid Interface Sci.* **1995**, *171*, 525.
[7] H. Ohshima, T.W. Healy, L.R. White, *J. Colloid Interface Sci.*, **1982**, *90*, 17.
[8] P. Attard, D. Antelmi, I. Larson, *Langmuir* **2000**, *16*, 1542.
[9] R. Tadmor, *J. Phys.: Condens. Matter* **2001**, *13*, 195.
[10] S. Kumagai, S. Yoshii, K. Yamada, N. Matsukawa, I. Fujiwara, *Appl. Phys. Lett.* **2006**, *88*, 153103.
[11] S. Biggs, P. Mulvaney, *J. Chem. Phys.* **1994**, *100*, 8501.
[12] D. Barten, J. M. Kleijn, J. Duval, H. P. von Leeuwen, J. Lyklema, M. A. C. Stuart, *Langmuir* **2003**, *19*, 1133.
[13] T. J. Davis, K. C. Vernon, D. E. Gómez, *Phys. Rev. B* **2009**, *79*, 155423.
[14] T. J. Davis, D. E. Gómez, K. C. Vernon, *Nano Lett.* **2010**, *10*, 2618.
[15] K. C. Vernon, A. M. Funston, C. Novo, D. E. Gómez, P. Mulvaney, T. J. Davis, *Nano Lett.* **2010**, *10*, 2080.
[16] U. Hohenester, A. Trugler. *Comput. Phys. Commun.* **2012**, *183*, 370.
[17] C. Novo, A. M. Funston, I. Pastoriza-Santos, L. M. Liz-Marzan, P. Mulvaney, *J. Phys. Chem.* C **2007**, *112*, 3.
[18] Y.Nishijima, L. Rosa, S. Juodkazis, *Appl. Phys. A* **2013**, *113*, 1.